THE JOURNAL OF PHYSICAL CHEMISTRY C

C: Plasmonics; Optical, Magnetic, and Hybrid Materials

Near Field Enhancement Contribution to the Photoactivity in Magnetite-Gold Hybrid Nanostructures

Federico Valentin Guzman, Pablo A. Mercadal, Eduardo A. Coronado, and Ezequiel Roberto Encina

J. Phys. Chem. C, **Just Accepted Manuscript** • DOI: 10.1021/acs.jpcc.9b09421 • Publication Date (Web): 20 Nov 2019

Near Field Enhancement Contribution to the Photoactivity in Magnetite-Gold Hybrid Nanostructures

Federico V. Guzman†, Pablo A. Mercadal†, Eduardo A. Coronado and Ezequiel R. Encina*

INFIQC-UNC-CONICET, Departamento de Fisicoquímica, Facultad de Ciencias Químicas, Universidad Nacional de Córdoba, Córdoba, 5000, Argentina

† These authors made equal contributions

* Corresponding author: Ezequiel R. Encina

e-mail address: ezencina@fcq.unc.edu.ar

Tel: +54-351-535-3866 Fax: +54-351-433-4180

Abstract

Hybrid nanostructures composed of magnetic iron oxides and plasmonic metals are able to convert light energy into chemical energy as well as they can be easily manipulated through magnetic fields. As a consequence of these multifunctional features they can be employed as magnetically recyclable heterogeneous photocatalysts. Herein, we report a two step method for the preparation of magnetite (Fe_3O_4)-gold (Au) hybrid nanostructures in aqueous media. The obtained material resembles a core-satellite morphology of 60 nm Fe_3O_4 nanoparticles surrounded by nearly spherical 20 nm Au nanoparticles attached to their surface. The synthesized hybrid material exhibits enhanced capabilities for the methylene blue photodegradation compared with bare Fe_3O_4 nanoparticles. Detailed electrodynamics simulations were performed to achieve further insight into the improved photoactive properties of the Fe_3O_4-Au hybrid nanostructures. The theoretical results show that the excitation of localized surface plasmon resonances in the Au component leads to greater light absorption in the Fe_3O_4 component which ultimately impacts on the improved photocatalytic properties of the hybrid nanostructure. Overall, this work provides a complementary approach toward a complete understanding of the enhanced photoactive properties of hybrid nanostructures and highlights the importance of considering their actual morphology into simulations.

Introduction

Hybrid nanostructures composed of metal oxides and noble metals (HNs) have been intensively investigated in the past years mainly because of their multifunctional characteristics, as they allow to integrate several physical and chemical properties into a single object.[1–5] Indeed, owing to its multifunctional features, HNs have been applied to address issues regarding from biomedicine to environmental remediation.[6–10] In particular, HNs composed of magnetite (Fe_3O_4) and gold (Au), exhibit both magnetic and plasmonic properties. As a consequence of the properties of its constitutive materials, this specific type of HN has shown a remarkable performance when employed as SERS substrates and as heterogeneous magnetically recyclable photocatalysts.[11–15] Although there still remain open questions, there exist consensus about the fundamental reasons that lead to improvements in the photocatalytic activity.[16–18] The intense electric field produced on the surface of the noble metal nanoparticle by localized surface plasmon resonance (LSPR) excitation significantly increases the electron-hole generation efficiency in the nearby semiconductor. This process occurs through a dipole-dipole coupling between the dipole moment of LSPR and the dipole moment of interband transitions in the semiconductor. This process resembles in some way the mechanism of Forster energy transfer (FRET) observed between donors and acceptor molecules, and it has been denoted as Plasmon Induced Resonance Energy Transfer (PIRET).[19–22] Optimization of this mechanism requires both spectral and spatial overlaps, that is, the excitation energy of the LSPR should be similar to the semiconductor bandgap. In addition, the semiconductor component must occupy the spatial region next to the plasmonic nanoparticle (NP) where the most substantial increase of the near-field occurs. Consequently, the generation of electron-hole pairs is located near the surface of the semiconductor, significantly reducing the recombination of charge carriers during their migration toward the catalytic sites at the interface.[23] Recently, we have shown by means of electrodynamics simulations that the absorbed photon flux within the semiconductor component of a given HN depends not only on the spectral overlap but also on the radiative line width of the plasmonic resonance, which in turn depends on the size and nature of the

plasmonic particle.[24] These results highlight that a rational design of the morphology of the HN is required in order to enhance its photoactive properties. The improvements in the photocatalytic properties of HNs composed of semiconductor metal oxides and noble metals with respect to those corresponding to photocatalysts composed purely of the semiconductor metal oxide are also attributed to a charge transfer mechanism.[25,26] Upon the excitation of the LSPR, a fraction of the hot electrons generated in the metal reaches high enough energy to overcome the Schottky barrier formed at the metal/semiconductor interface and is injected into the conduction band of the semiconductor.[27] This mechanism further enhances the separation of electrons and holes, which in turn reduces the recombination rate and increases the lifetime of charge carriers. Importantly, the occurrence of the hot electron injection process is heavily dictated by the Fermi energy level, while the PIRET mechanism implies less exigent conditions.

In general, the methods reported for the preparation of Fe_3O_4-Au HNs involve two steps, first the synthesis of Fe_3O_4 NPs followed by the reduction of Au(III) ions in presence of Fe_3O_4 NPs obtained in the first step. The most widely applied protocols for the synthesis of Fe_3O_4 NPs comprise either the co-precipitation method, approach involving solvothermal and high-temperature reactions or partial oxidation of Fe(II) solutions.[28–30] On the one hand, the co-precipitation method at ambient conditions is simple but the control of the size and shape distributions is relatively poor.[31,32] On the other hand, the methods that involve hydrothermal and high-temperature reactions are more sophisticated but leads to very good shape control as well as to very narrow size distributions typically centered below 20 nm, that is, within the superparamagnetic size regime.[33] The partial oxidation of dissolved Fe(II), and the subsequent formation of the desired solid phase, has also been intensively studied and it likely constitutes the most inexpensive methodology for the preparation of Fe_3O_4 NPs.[34,35] The reduction of Au(III) ions is usually accomplished by using sodium borohydride, sodium citrate and hydroxylamine hydrochloride.[36,37] Furthermore, according to the surface functionalization of the Fe_3O_4 NPs and to specific details of the synthetic procedure, Fe_3O_4-Au HNs with two main different morphologies can be obtained: core-shell or core-satellite.[38] Regarding the enhanced NHs photocatalytic properties different

combinations have been investigated using Fe_3O_4, TiO_2 and other components as dielectric materials with Au, demonstrating their capabilities to produce the photodegradation of organic compounds such as 4-nitrophenol and dyes.[39] However, to the best of our knowledge, the photocatalytic properties of HNs composed solely by Fe_3O_4 and Au have not been addressed yet. This simple two component system allows us to achieve a deeper comprehension of the photocatalytic activity using electrodynamics modelling, an aspect quite relevant but scarcely employed to explain experiments.[40]

In this work, Fe_3O_4-Au HNs has been prepared by implementing a relatively simple two step method. In a first step, Fe_3O_4 NPs are obtained by aerial oxidation of $Fe(OH)_2$ suspensions. This procedure constitutes an environmental friendly and low cost method for the preparation of Fe_3O_4. The formation of Fe_3O_4-Au HNs is obtained in a second step, by heterogeneous precipitation of Au on the surface of the Fe_3O_4 NPs, reducing Au(III) ions with borohydride. The structure and morphology of the prepared HNs were characterized by TEM, SEM, EDS and XRD. Then, the photocatalytic properties of the Fe_3O_4-Au HNs were also investigated by analyzing the photodegration of the methylene blue dye (MB) followed by UV-vis spectroscopy. Finally, based on detailed Discrete Dipole Approximation (DDA) simulations, the enhancement in the photoactive response of the HNs is qualitatively rationalized according to the near field enhancements in the semiconductor material.

Experimental and Theoretical Methods

Chemicals. Ferrous sulfate ($FeSO_4 \cdot 7H_2O$, Anedra), sodium hydroxide (NaOH, Anedra), tetrachloroauric acid ($HAuCl_4 \cdot 3H_2O$, Sigma-Aldrich), sodium borohydride (Tetrahedron) and methylene blue (MB, Sigma-Aldrich), reagents of high purity grade, were used as received without further purification. Aqueous solutions were prepared with ultrapure water (18.2 mΩ resistivity).

Synthesis of Fe_3O_4 Nanoparticles. The synthesis of Fe_3O_4 NPs was performed by adding 100 mL of a freshly prepared 0.1 M $FeSO_4$ solution to 100 mL of a 0.4 M NaOH solution under vigorous stirring at

room temperature. After mixing the reactants the temperature was set to 80º C during an hour. At the end of this period a black precipitated was obtained indicative of Fe_3O_4 formation.

Synthesis of Fe_3O_4-Au Hybrid Nanostructures. The HNs were obtained by mixing 0.1 mL of a 0.025 M $HAuCl_4$ solution with 10 mL of a 0.05 g/L Fe_3O_4 NPs aqueous dispersion. Then, four aliquots of 0.015 mL each one of a fresh $NaBH_4$ 0.1 M solution were added to this mixture, under vigorous stirring. After adding the $NaBH_4$ aliquots, the appearance of a purplish color was observed in the reaction mixture, suggesting the formation of Au NPs. This color was quite different to the typical red color of Au NPs dispersions observed in control experiments where the same procedure was performed in the absence of Fe_3O_4 NPs.

XRD Characterization. The XRD instrument employed was a PANanalitical X-Pert Pro using CuKα radiation (λ =1.5406 Å). The diffractograms were obtained from powders of the respective samples in the range 20−80°. To obtain the powder of Fe_3O_4 NPs, the suspension containing the reaction product was washed three times with water and the precipitated NPs were dried in an oven overnight at 40 °C. The respective powder of the Au-Fe_3O_4 HNs sample was obtained by depositing droplets containing the nanostructures over a glass slide, and evaporating the solvent in a fumehood at room temperature.

TEM, SEM and EDS Characterization. Transmission electronic microscopy (TEM) images of the prepared nanostructures were obtained by using a JEM-JEOL 1120 EXII under an accelerating voltage of 80 kV, whereas the samples were prepared by adding one drop (~30 μL) of the colloidal dispersion onto a holey carbon-formvar coated copper TEM grid (100 mesh). Scanning electronic microscopy (SEM) images of the prepared nanostructures were obtained by using a FE-SEM Σigma (Carl Zeiss), whereas the samples were deposited onto Si/SiO2 substrates. The analysis of the chemical composition of the respective samples was performed by energy dispersive X-ray spectroscopy (EDS, Oxford).

UV−Vis Spectroscopy. The spectra were measured at room temperature using a Shimazdu UV-1700 PharmaSpec spectrophotometer with a cuvette of 1 cm optical path length.

Photocatalysis experiments. The synthesized Fe_3O_4 NPs and Au-Fe_3O_4 HNs were tested for the photocatalytic degradation of methylene blue (MB). The photocatalysis experiments were carried out in a test tube containing 10 mL of $1x10^{-5}$ M MB solution and 0.083 mg/L of the respective catalyst. Before start the irradiation, the suspension was magnetically stirred for 1 h in order to attain adsorption-desorption equilibrium. The experiments were performed by irradiating the samples with a 100 W Hg lamp as light source. At specific time intervals (15 m), 2 mL of the sample solution were withdrawn and the changes in the concentration of MB were monitored through UV-vis measurements.

Computational Methods. The absorption spectra of Fe_3O_4 and Fe_3O_4-Au nanostructures as well as the near field enhancements were calculated using the DDA method which is implemented in the DDSCAT 7.3 code.[41] Further details about this methodology can be found elsewhere.[42,43] The synthesized Fe_3O_4-Au HNs were modelled as core-satellite like objects. The dimensions of the Fe_3O_4 core and of the Au satellite nanoparticles were taken from the size distribution statistics obtained from the TEM images (see Figure 2). The number of dipoles N used to represent a given nanostructure is a key parameter when performing DDA simulations as both the accuracy of the simulation and the computational time, increase with N. Thus, N should be chosen in such a way as to reach an acceptable error tolerance. Note that there exists an inversely proportional relationship between the lattice spacing and N, that is, the smaller the lattice spacing the larger N. The value of N employed to model the synthesized nanostructures in the simulations was varied from 1.1×10^5 to 1.4×10^5 according to the actual dimensions in such a way that a lattice spacing (inter-dipole distance) of 1 nm was set in all simulations. The wavelength dependent dielectric constant of Fe_3O_4 and Au were obtained from literature.[44,45] The refractive index of the environment was set to 1.33 corresponding to water.

Results and discussion

Structural characterization. The structure and nature of the synthesized materials has been characterized through XRD measurements. Figure 1 shows the XRD patterns of the powders obtained from the Fe_3O_4 NPs and Au-Fe_3O_4 HNs denoted as (a) and (b), respectively. For comparison, the reference data for Fe_3O_4 (ICSD 01-089-0691) and Au (ICSD 03-065-2870) are also shown at the bottom as red and blue bars, respectively. The diffraction pattern of (a) Fe_3O_4 NPs shows peaks at 2θ = 30.2, 35.6, 37.3, 43.2, 53.7, 57.2, and 62.8, which are assigned to the reflections of the planes (220), (311), (222), (400), (422), (511), and (440) of Fe_3O_4, respectively. Note that diffraction peaks that could be attributed to other iron oxide or oxyhydroxide phases are not observed indicating that there are no other impurities in the Fe_3O_4 NPs.

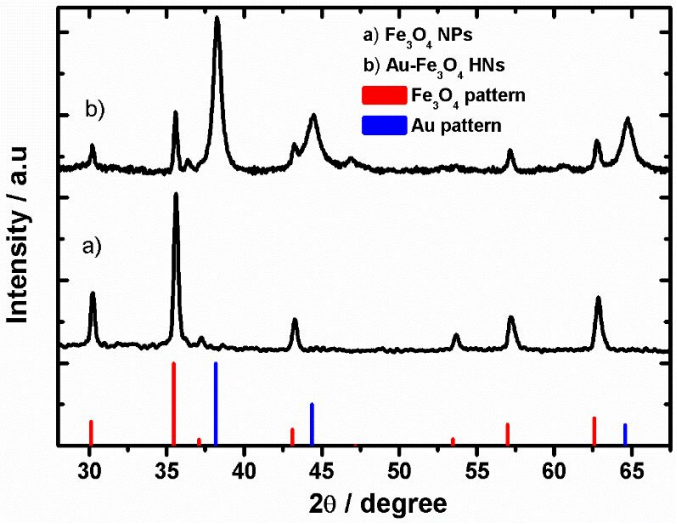

Figure 1. XRD patterns of (a) Fe3O4 NPs and (b) Fe3O4-Au HNs. The reference XRD pattern of Fe3O4 (ICSD 01-089-0691) and Au (ICSD 03-065-2870) are also shown in the lower part of the figure in red and blue bars, respectively. The patterns have been arbitrarily shifted in the y-axis.

On the other hand, the diffraction pattern of (b) Au-Fe_3O_4 HNs shows peaks at 2θ = 38.2, 44.5 and 64.7 which are assigned to the reflections of the planes (111), (200), and (220) of Au, respectively, in addition to the peaks attributed to reflections of the Fe_3O_4 phase. This analysis suggests that the implemented methodology is suitable for the preparation of Fe_3O_4-Au HNs.

Morphological and elemental characterization. Figure 2 shows representative TEM images of the synthesized (a) Fe_3O_4 NPs and (b) Fe_3O_4-Au HNs, respectively. It is observed that the prepared Fe_3O_4 NPs present relatively wide shape and size distributions (Fig. 2a). Given the crystalline nature of the Fe_3O_4 nanoparticles shown in Fig. 2a, the different contrast observed could be attributed to diffraction contrast.

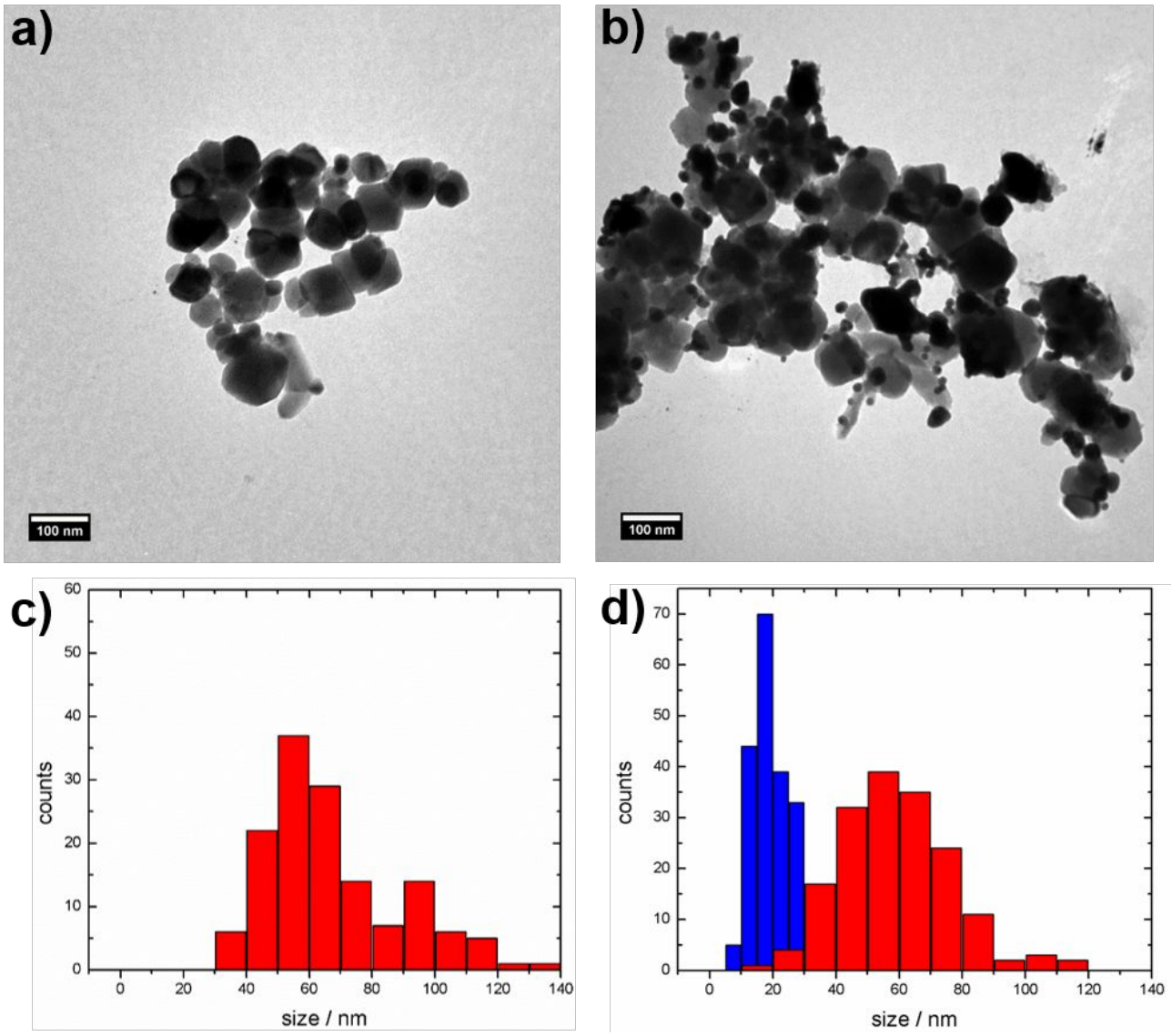

Figure 2. (a-b) Representative TEM images of the synthesized (a) Fe_3O_4 NPs and (b) Fe_3O_4-Au HNs. (c-d) Histograms of the particle size distribution of (c) Fe_3O_4 NPs and (d) Fe_3O_4-Au HNs. In panel (d), red bars correspond to the size of the Fe_3O_4 whereas the blue bars correspond to the size of the Au component of the NH, respectively.

However, a contribution of mass-thickness contrast to the image formation can not be ruled out due to the fact that the thickness of the specimen is inhomogeneous. The shape and size distributions can be attributed to the formation process of the magnetic iron oxide phase. Note that, according to the methodology employed, the Fe_3O_4 formation involves several different steps, including the initial formation of $Fe(OH)_{2(s)}$, the following conversion into green rust, its dissolution and finally the precipitation of Fe_3O_4. The final size and shape distributions of the NPs obtained greatly depend on whether the Fe_3O_4 crystal growth follows classical or non-classical mechanisms. Indeed, all the above mentioned phenomena should have an impact on the product; however, determining the crystal growth mechanism and the key variables that control the Fe_3O_4 formation is beyond the scope of this work. The statistical analysis of the images, performed on the basis of counting over hundred particles, reveals that the mean size of the Fe_3O_4 NPs is centered around 60 nm (Fig. 2c). Figure 2b shows a representative TEM images of the synthesized Fe_3O_4-Au HNs where it can be clearly appreciated the presence of small and nearly spherical particles with substantially high electronic contrast attributed to Au NPs surrounding a core with relatively lower contrast corresponding to Fe_3O_4. Furthermore, the Au NPs appears to be randomly distributed on the surface of the Fe_3O_4 NPs resembling the so-called core-satellite morphology employed in literature to describe this type of HN. The statistical analysis of the respective TEM images indicates that the size distribution of the Fe_3O_4 NPs remains practically unchanged after the process that leads to the formation of the HNs, that is, the heterogeneous nucleation and subsequent growth of Au over the Fe_3O_4 surface (see red bars in the histogram depicted in Fig. 2d). In addition, according to the respective statistical analysis, the Au NPs depict a narrower size distribution centered at 20 nm (see blue bars in the histogram depicted in Fig. 2d). These morphological features have been also verified trough SEM images, where it can be clearly observed that the initial Fe_3O_4 NPs (Fig. 3a) are modified by the deposition of smaller Au NPs on their surface after producing the reduction of Au(III) ions by reaction with $NaBH_4$ (Fig. 3b). Note that some of the Au NPs that compose the HNs are illustratively indicated by red arrows in Fig. 3b.

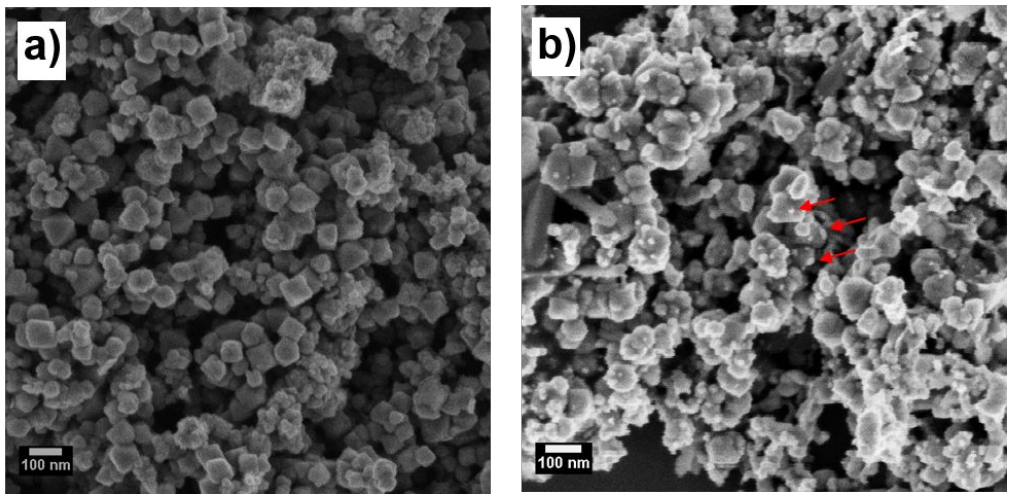

Figure 3. Representative SEM images of the synthesized (a) Fe_3O_4 NPs and (b) Fe_3O_4-Au HNs. Red arrows in panel (b) illustratively indicate some Au NPs that compose the HNs.

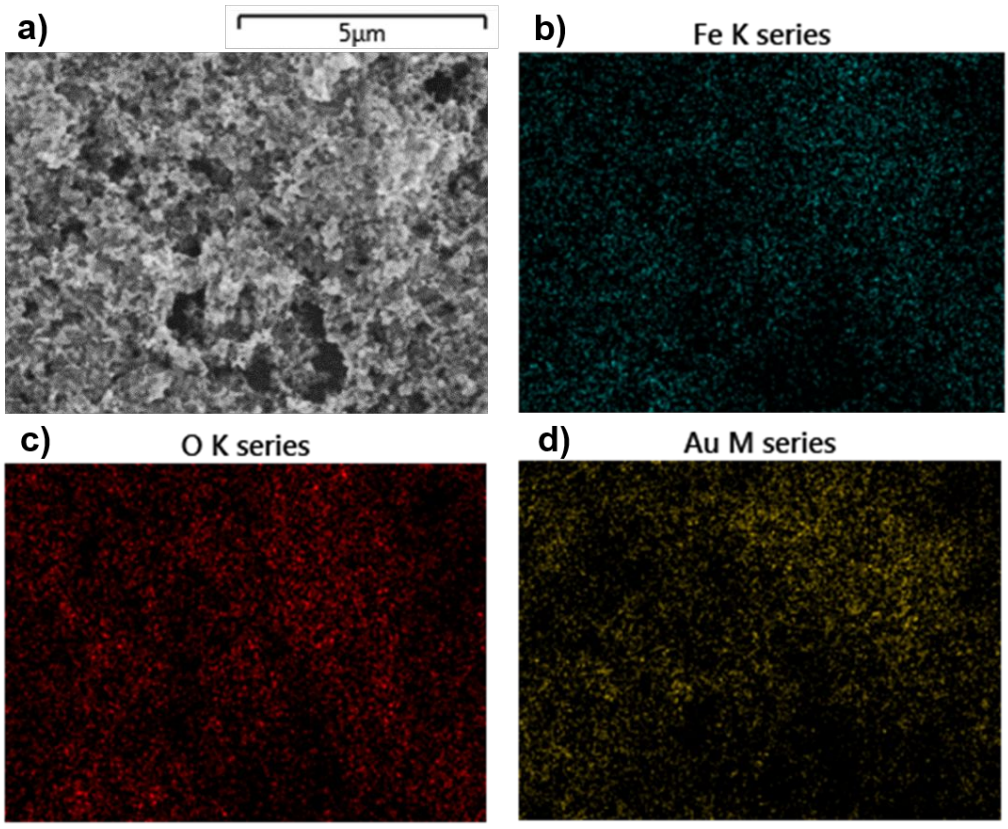

Figure 4. (a) SEM image and EDS element mapping images for (b) Fe, (c) O and (d) Au of the synthesized Fe_3O_4-Au HNs. The scale bar applies for all images.

The chemical composition analysis of the synthesized materials was performed by means of EDS measurements. Figure 4a depicts a representative SEM image of the Fe_3O_4-Au HNs, while the corresponding EDS element mapping images presented in Figs. 4b, 4c and 4d provide evidence that the synthesized HNs are composed of Fe, O and Au, respectively, with these elements being homogenously distributed in the material. The respective EDS spectrum is provided in Fig. S1 of the Supporting Information (SI) file and substantiates that the synthesized composite is constituted of Fe, O, and Au. The EDS analysis for the Fe_3O_4 NPs sample is provided in Fig. S2 of SI, where it can be clearly appreciated the presence of signals corresponding only to Fe and O and, in contrast, the absence of signals corresponding to Au can be corroborated.

Optical characterization. Owing to the plasmonic properties of noble metals, it is expected that the optical response of the Fe_3O_4 NPs substantially change after the heterogeneous precipitation of Au on their surface, that is, after the formation of the Fe_3O_4-Au HNs. Figure 5 shows the normalized extinction spectrum of the aqueous dispersion of the synthesized Fe_3O_4 NPs which resembles the typical spectrum previously obtained for colloidal dispersions of this material (black curve).[46–48]

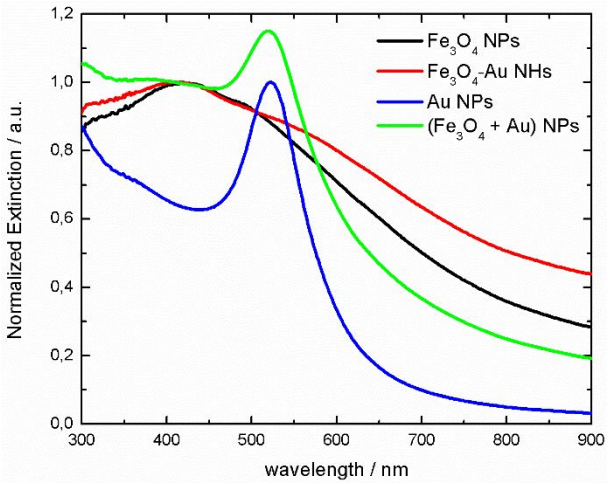

Figure 5. Normalized extinction spectra corresponding to colloidal dispersions of the synthesized Fe_3O_4 NPs (black curve), Fe_3O_4-Au HNs (red curve) and Au NPs (blue curve). The green curve shows the spectrum resulting from the averaged sum of the individual spectra of Fe_3O_4 and Au NPs, normalized at 411 nm.

The corresponding spectrum of the Fe_3O_4-Au HNs (red curve) depicts a shoulder around 560 nm superimposed on the spectrum of the Fe_3O_4 NPs. This response is attributed to the excitation of the LSPR of the Au component of the HNs. Besides, there is an increased extinction in the 300-400 nm range attributed to inter-band transition of Au. In order to achieve deeper insight into this response, the normalized extinction spectrum of Au NPs (obtained following the same procedure employed to prepare the HNs but without Fe_3O_4 NPs dispersed in the reaction media) is shown in blue curve. Such a spectrum presents a remarkable peak at 522 nm characteristic of Au NPs colloidal dispersions attributed to LSPR excitations. A representative TEM image of the Au NPs produced in the absence of Fe_3O_4 is shown in Fig. S3 of SI. The statistical analysis indicates that the Au NPs exhibit a nearly spherical shape with a mean size of 20 nm and size and shape distributions quite similar to those obtained for the Au component of the HNs. However, the shoulder observed in the HNs extinction spectrum, which appears as a consequence of LSPR excitations in the Au component, is nearly 40 nm red-shifted with respect to the respective peak of the naked Au NPs. This effect is attributed to the higher dielectric constant of the environment experienced by the Au component in the HN, and provides an additional evidence of the close interaction between Fe_3O_4 and Au materials. Furthermore, in virtue of this interaction, the spectrum resulting from the sum of the individual spectra of Fe_3O_4 and Au NPs (green curve), substantially differs from that obtained for the Fe_3O_4-Au HNs (red curve). Note that, to give a clear comparison, the spectrum shown in green curve is obtained by normalizing at 411 nm the averaged sum of the respective spectra of Fe_3O_4 and Au NPs. As mentioned before, it is expected that the LSPR excitations have an impact on the photoactive properties of the HNs.

Photocatalytic degradation of MB. The dye MB was employed as probe molecule for evaluating the photocataytic performance of the synthesized materials. Figure 6a shows the variation of the absorption spectrum of MB with irradiation time in presence of Fe_3O_4-Au HNs. It can be observed that the intensity of the absorption peak at 664 nm of MB continuously decreases as the irradiation time increases from 0 to 60 minutes, a process evidenced by the discoloration of the dye. For comparison, the

photodecomposition of the dye in presence of Fe_3O_4 NPs and without any photocatalyst, that is, an aqueous solutions of MB, were also investigated. The absorption spectrum of MB at different irradiation times is shown in Figs. S4a and S4b of SI, respectively. In this case, there is qualitatively the same trend observed in Fig. 6a. The variation of the MB normalized absorption valuated at 664 nm, I_t/I_0, with the irradiation time is shown in Fig. 6b. Green dots (red dots) represent data measured in presence of Fe_3O_4-Au HNs (Fe_3O_4 NPs), while black dots represent data of control experiments performed for MB aqueous solutions without photocatalyst. After an hour of irradiation, the MB concentration decreases to 30% from its initial value in the absences of photocatalysts. By performing the same experiment in presence of Fe_3O_4 NPs, the photodegradation process of MB is accelerated and after 60 minutes of irradiation the MB concentration reaches a 25% of its initial value. However, when Fe_3O_4-Au HNs are present in the reaction media the MB photodecomposition is further enhanced and it decreases to 10% of its initial concentration after the same period of time.

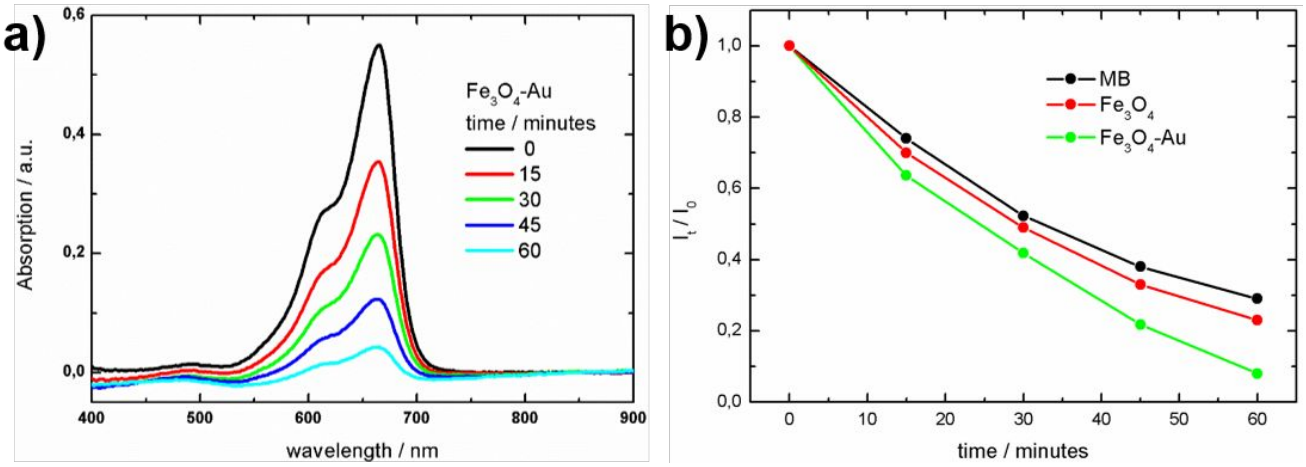

Figure 6. a) Absorption spectrum of MB at different irradiation times in presence of the synthesized Fe_3O_4-Au HNs. b) Variation of the MB normalized absorption with the irradiation time in presence of Fe_3O_4 NPs (red dots) and Fe_3O_4-Au HNs (green dots). Data of control experiments performed for MB solutions are shown in black dots.

The increased photocatalytic activity of Fe_3O_4-Au HNs with respect to Fe_3O_4 NPs is attributed to the plasmonic properties of the Au component which gives place to two main phenomena: charge

transference trough the Schottky barrier and larger absorption in the Fe_3O_4 core that ultimately increases the electron-hole pair generation process. The variables that control the possible plasmonic enhancement mechanisms for extending photoconversion, that is, PIRET and hot carriers transfer are spectral overlap and contact between the metal/semiconductor surface, respectively. Therefore, it is expected that both mechanisms occurs simultaneously in the fabricated Fe_3O_4-Au materials. In this regard, based on transient absorption spectroscopy and theoretical calculations, Wu and co-workers have suggested that, in samples with large spectral overlaps, the overall enhancement is dominantly from PIRET.[49] This claim is further supported by the fact that the transfer efficiency of hot electrons is usually <10% of absorbed light, whereas the near field transfer efficiency can approach that of the semiconductor absorbing light on its own.[26] By applying this reasoning to the fabricated material in this work, it would be expected that PIRET would dominate the observed enhancement in the photoactivity. The electrons and holes generated in the conduction and valence band of the semiconductor, can induce redox reactions with other species present in the system producing reactive oxygen species that then react with the dye to form oxidized products and are thus responsible for its photodegradation. It is well known that Au NPs supported on metal oxides exhibit catalytic activity in several chemical transformations.[50] In some cases, it has been argued that the support could act actively in the reaction mechanism by redox cycling of the support metal ions, being MnO_2, CeO_2 and Fe_2O_3 representative examples.[51] Thus, it has been suggested that the participation of the metal oxide support in the reaction mechanism would enhance the catalytic activity of the Au NPs due to stabilization of positive gold species. Furthermore, it has been proposed that such a cooperation between the support and the Au NPs in the catalytic cycle might explain different catalytic performances of Au NPs when supported on distinct metal oxides.[52] Therefore, considering these properties, additional experiments under identical experimental conditions to those presented in Fig. 6a but without illumination have been performed. The results obtained clearly show that the absorption spectrum of MB remains practically unchanged after several hours without illumination (see Fig. S5). These data provide further evidence that it is indeed the energy transfer the responsible for the

photocatalytic rate enhancement and not the direct catalysis on Au surface. In the following, focus will be made in the light absorption of the Fe_3O_4 core to provide a partial explanation for the enhanced photoactivity observed in presence of Fe_3O_4-Au HNs.

Electrodynamics simulations. DDA simulations have been performed in order to achieve further insight into the enhanced photocatalytic activity of the Fe_3O_4-Au HNs. Figure 7a shows a representative TEM image of the synthesized Fe_3O_4-Au HNs where it can be appreciated in more detail that it resembles a core-satellite morphology. Therefore, based on this morphological characterization, we have used as prototype for modelling the optical properties a 60 nm diameter Fe_3O_4 sphere decorated by six 20 nm diameter Au hemispheres at right angles from each other, that is, oriented along the ±x, ±y and ±z directions, the origin of the coordinate system being at the center of the Fe_3O_4 sphere as shown in Fig. 7b.

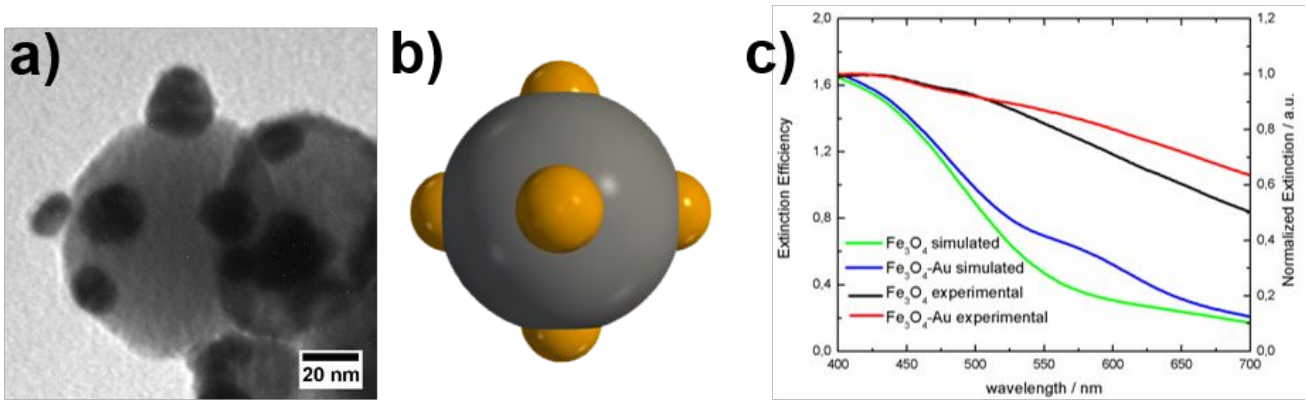

Figure 7. a) Representative TEM image of the synthesized Fe_3O_4-Au HNs and b) the graphical representation of the computational model employed to simulate its optical properties. c) Simulated extinction efficiency spectrum of Fe_3O_4 NPs (green curve) and of Fe_3O_4-Au HNs (blue curve) (left y-axis). The dimensions of the computational nanostructures are detailed in the text. Experimental normalized extinction spectrum of colloidal dispersions of Fe_3O_4 NPs (black curve) and of Fe_3O_4-Au HNs (red curve) (right y-axis).

A comparison of the simulated extinction efficiency of a 60 nm diameter Fe_3O_4 sphere and of the above mentioned HN is shown in green and blue curves of Fig. 7c, respectively. The extinction efficiency values for the Fe_3O_4 nanosphere (green curve) are relatively large near 400 nm, considerably decrease from 450

to 550 nm, and remain approximately constant between 600 and 700 nm. On the other hand, the extinction efficiency spectrum of the Fe_3O_4-Au HN (blue curve) displays similar features but, in addition, it shows a pronounced shoulder at 560 nm. Importantly, the simulated spectra capture the most relevant features observed in the experimental spectra of colloidal dispersions of Fe_3O_4 NPs and Fe_3O_4-Au HNs, standing out the enhanced extinction of the HNs with respect to bare Fe_3O_4 NPs (depicted with the black and red curves in Fig. 7c, respectively). Note that additional simulations shown in Fig. S6 of SI provide evidence that the lattice spacing value of 1 nm is good enough to give accurate results. These findings suggest that this morphologically simplified model nanostructure is suitable for simulating the optical properties of the synthesized HNs. The quantitative differences between simulated and experimental spectra can be attributed to two main sources. On the one hand, the size and shape inhomogeneity of the synthesized nanostructures leads to spectral broadening of extinction. Simulated extinction efficiency spectra of different size and shape Fe_3O_4 nanoparticles shown in Fig. S7 support this statement. On the other hand, the presence of larger aggregates formed by several HNs give rise to higher scattering cross sections than isolated HNs, a feature that partially explains the larger measured extinction values. This effect has not been taken into account in the simulated spectrum for a single HN. The inhomogeneity in the size and shape as well as the presence of larger size aggregates in the aqueous dispersion are supported by the respective TEM and SEM images.

Besides extinction and scattering efficiencies, the absorption efficiency is the most useful quantity to analyze the photocatalytic properties of the Fe_3O_4-Au NHs. Figure 8 compares the absorption efficiency spectrum of a 60 nm diameter Fe_3O_4 sphere (black dashed curve) with the previously described HN (black curve). The spectra are quite similar to the extinction efficiency spectra shown in Fig. 7c given that the scattering efficiency values for this single HN are small and nearly constant in the wavelength range studied. By applying eq. (1) reported in ref. 24, it was possible to calculate the absorption efficiency spectrum for each component of the HN, that is, the partial contributions from the Au and Fe_3O_4 components. In particular, the absorption efficiency spectrum of the Au component of the HN (Fig. 8,

blue curve) presents a broad peak centered at 570 nm which is attributed to the LSPR excitation. On the other hand, the absorption efficiency spectrum of the Fe_3O_4 component (Fig. 8, red curve) is qualitatively quite similar to that one of the 60 nm diameter Fe_3O_4 nanosphere (Fig. 8, black dashed curve). However, it can be clearly observed that the absorption efficiency values for the Fe_3O_4 component of the HN are notably larger than the corresponding values for the naked Fe_3O_4 nanosphere in the 500-650 nm wavelength range. Interestingly, this wavelength range overlaps with the excitation wavelength of the LSPRs in the Au component of the HN suggesting that an energy transfer mechanism should be involved.

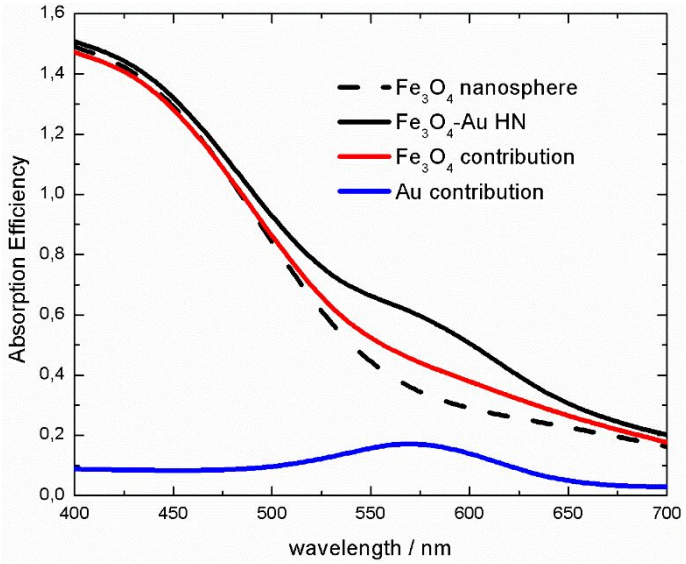

Figure 8. a) Simulated absorption efficiency spectrum of Fe_3O_4-Au NHs (black curve) along with the respective contributions from the Fe_3O_4 (red curve) and Au (blue curve) components. Black dashed curve shows the simulated absorption efficiency of a Fe_3O_4 nanosphere with equal radius to that one that compose the Fe_3O_4-Au HN. Details about the specific dimensions of the nanostructures are provided in the text.

The enhanced light absorption, and the consequent improved electron-hole generation, in the Fe_3O_4 component of the HNs partially explains its increased photocatalytic activity, as the process such as charge transfer processes that might certainly take place upon the LSPR excitation, were not taken into account.

The near field enhancements generated by the LSPR excitation in the Au component of the HN produce larger electric fields within the Fe_3O_4 component which in turn give place to greater absorption

efficiency. This effect of the plasmonic Au component on the absorption properties of the Fe_3O_4 component can be further appreciated in Fig. 9 comparing the near field enhancement values for a 60 nm diameter Fe_3O_4 nanosphere (panel (a)) with the already described HN (panel(b)) both along the y-z plane and x=0. In this set of calculations the incident light, with a wavelength of 570 nm, propagates along the x-axis and it is linearly polarized along the y-axis. The value of electric field enhancement is practically the same within the naked Fe_3O_4 nanosphere (panel (a)), while as a consequence of LSPR excitations of the Au component in the HN, the near field enhancement distribution changes.

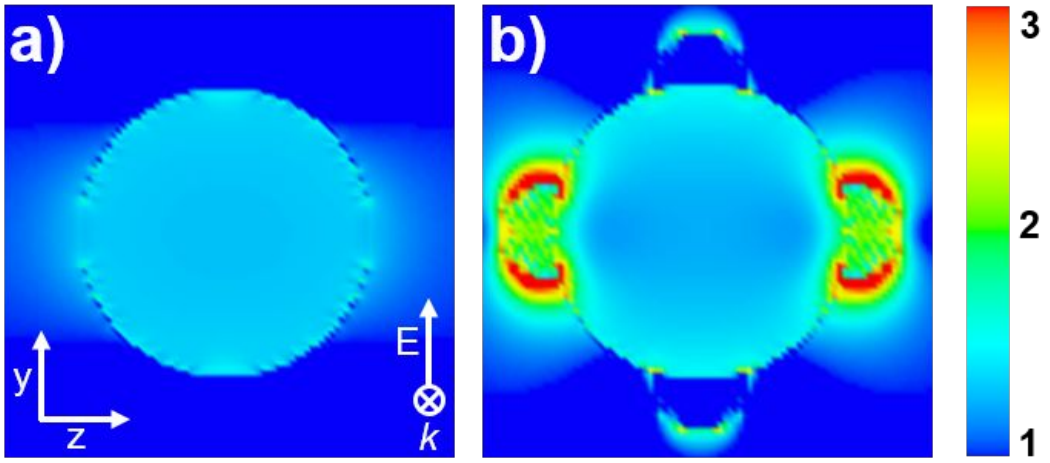

Figure 9. Near field enhancement values for a 60 nm diameter Fe_3O_4 nanosphere (a) and for a Fe_3O_4-Au HN (b), in the y-z plane (x=0). Dimensions of the HN are described in the text. The incident light, with a wavelength of 570 nm, propagates along the x-axis and it is linearly polarized along the y-axis. The intensity scale bar applies for both panels.

The regions of enhancement are produced not only in the Au local environment but also within the Fe_3O_4 core, particularly in those regions closer to the plasmonic structures. Consequently, the field enhancements produced by the Au component leads to enhanced light absorption in the Fe_3O_4 core.

Conclusions

In this work, a simple two step synthetic methodology have been implemented that allows to obtain Fe_3O_4-Au HNs in aqueous media. In particular, the obtained HNs are mainly compose of a Fe_3O_4 core, with a mean size of 60 nm, decorated by nearly spherical Au NPs having a mean size of 20 nm. It has been found that the prepared material presents improved photocatalytical properties toward the photodegradation of methylene blue with respect to pure Fe_3O_4 NPs, the enhanced photoactivity being attributed to LSPR excitations in the Au component of the HN. Furthermore, the determined morphological characteristics for the Fe_3O_4 NPs and Fe_3O_4-Au HNs were employed to simulate their absorption spectra by means of rigorous DDA simulations. The qualitative good agreement obtained between experimental and theoretical extinction spectra indicates that the simplified model of the nanostructure employed capture the most significant morphological features of the synthesized HNs and it is suitable for simulating their optical properties. It has been shown that the enhanced absorption efficiency in the Fe_3O_4 component of the HN with respect to an equal size Fe_3O_4 NP is due to near field enhancements that arises ultimately as a consequence of LSPR excitations in the plasmonic Au component. The improved photocatalytical performance found for the HNs is attributed in part to the enhanced absorption efficiency in the Fe_3O_4 component of the HN, besides the hot electron injection processes that might certainly take place upon the LSPR excitation. The results presented here provide further insight for a deeper comprehension of the enhanced photoactive properties of HNs and highlights the importance of considering their actual morphology into simulations.

Supporting Information

EDS spectrum of the Fe_3O_4-Au HNs, SEM image and EDS element mapping images of Fe_3O_4, TEM image of Au NPs synthesized in absence of Fe_3O_4 NPs along with their respective size histogram, absorption spectrum of MB at different irradiation times in presence of Fe_3O_4 NPs and without any photocatalyst, absorption spectrum of MB at different times in presence of the synthesized Fe_3O_4–Au

HNs without illumination, simulated extinction, absorption and scattering efficiencies modeled with a lattice spacing of 1 nm and 0.5 nm, simulated extinction efficiency spectra of Fe_3O_4 nanospheres with different diameters and of a 60 nm side Fe_3O_4 nanocube.

Acknowledgments

This work was supported by the Agencia Nacional de Promoción Científica y Tecnológica (Préstamo BID PICT 2016 no. 1768).

References

(1) Carbone, L.; Cozzoli, P. D. Colloidal Heterostructured Nanocrystals: Synthesis and Growth Mechanisms. *Nano Today* **2010**, *5* (5), 449–493. https://doi.org/10.1016/j.nantod.2010.08.006.

(2) Ghosh Chaudhuri, R.; Paria, S. Core/Shell Nanoparticles: Classes, Properties, Synthesis Mechanisms, Characterization, and Applications. *Chem. Rev.* **2012**, *112* (4), 2373–2433. https://doi.org/10.1021/cr100449n.

(3) Kochuveedu, S. T.; Jang, Y. H.; Kim, D. H. A Study on the Mechanism for the Interaction of Light with Noble Metal-Metal Oxide Semiconductor Nanostructures for Various Photophysical Applications. *Chem. Soc. Rev.* **2013**, *42* (21), 8467. https://doi.org/10.1039/c3cs60043b.

(4) Encina, E. R.; Pérez, M. A.; Coronado, E. A. Synthesis of Ag@ZnO Core–Shell Hybrid Nanostructures: An Optical Approach to Reveal the Growth Mechanism. *J. Nanoparticle Res.* **2013**, *15* (6), 1688. https://doi.org/10.1007/s11051-013-1688-0.

(5) Jiang, R.; Li, B.; Fang, C.; Wang, J. Metal/Semiconductor Hybrid Nanostructures for Plasmon-Enhanced Applications. *Adv. Mater.* **2014**, *26* (31), 5274–5309. https://doi.org/10.1002/adma.201400203.

(6) Sotiriou, G. A.; Starsich, F.; Dasargyri, A.; Wurnig, M. C.; Krumeich, F.; Boss, A.; Leroux, J.-C.; Pratsinis, S. E. Photothermal Killing of Cancer Cells by the Controlled Plasmonic Coupling

of Silica-Coated Au/Fe 2 O 3 Nanoaggregates. *Adv. Funct. Mater.* **2014**, *24* (19), 2818–2827. https://doi.org/10.1002/adfm.201303416.

(7) Chen, X.; Li, G.; Han, Q.; Li, X.; Li, L.; Wang, T.; Wang, C. Rational Design of Branched Au-Fe 3 O 4 Janus Nanoparticles for Simultaneous Trimodal Imaging and Photothermal Therapy of Cancer Cells. *Chem. - A Eur. J.* **2017**, *23* (68), 17204–17208. https://doi.org/10.1002/chem.201704514.

(8) Wang, C.; Astruc, D. Nanogold Plasmonic Photocatalysis for Organic Synthesis and Clean Energy Conversion. *Chem. Soc. Rev.* **2014**, *43* (20), 7188–7216. https://doi.org/10.1039/C4CS00145A.

(9) Liu, X.; Iocozzia, J.; Wang, Y.; Cui, X.; Chen, Y.; Zhao, S.; Li, Z.; Lin, Z. Noble Metal–Metal Oxide Nanohybrids with Tailored Nanostructures for Efficient Solar Energy Conversion, Photocatalysis and Environmental Remediation. *Energy Environ. Sci.* **2017**, *10* (2), 402–434. https://doi.org/10.1039/C6EE02265K.

(10) Meng, X.; Liu, L.; Ouyang, S.; Xu, H.; Wang, D.; Zhao, N.; Ye, J. Nanometals for Solar-to-Chemical Energy Conversion: From Semiconductor-Based Photocatalysis to Plasmon-Mediated Photocatalysis and Photo-Thermocatalysis. *Adv. Mater.* **2016**, *28* (32), 6781–6803. https://doi.org/10.1002/adma.201600305.

(11) Leung, K. C.-F.; Xuan, S.; Zhu, X.; Wang, D.; Chak, C.-P.; Lee, S.-F.; Ho, W. K. W.; Chung, B. C. T. Gold and Iron Oxide Hybrid Nanocomposite Materials. *Chem. Soc. Rev.* **2012**, *41* (5), 1911–1928. https://doi.org/10.1039/C1CS15213K.

(12) Wang, D.; Astruc, D. Fast-Growing Field of Magnetically Recyclable Nanocatalysts. *Chem. Rev.* **2014**, *114* (14), 6949–6985. https://doi.org/10.1021/cr500134h.

(13) Moraes Silva, S.; Tavallaie, R.; Sandiford, L.; Tilley, R. D.; Gooding, J. J. Gold Coated Magnetic Nanoparticles: From Preparation to Surface Modification for Analytical and Biomedical Applications. *Chem. Commun.* **2016**, *52* (48), 7528–7540.

https://doi.org/10.1039/C6CC03225G.

(14) Encina, E. R.; Coronado, E. A. Size Optimization of Iron Oxide@Noble Metal Core–Shell Nanohybrids for Photothermal Applications. *J. Phys. Chem. C* **2016**, *120* (10), 5630–5639. https://doi.org/10.1021/acs.jpcc.5b11030.

(15) Canet-Ferrer, J.; Albella, P.; Ribera, A.; Usagre, J. V.; Maier, S. A. Hybrid Magnetite–Gold Nanoparticles as Bifunctional Magnetic–Plasmonic Systems: Three Representative Cases. *Nanoscale Horizons* **2017**, *2* (4), 205–216. https://doi.org/10.1039/C6NH00225K.

(16) Zhou, N.; López-Puente, V.; Wang, Q.; Polavarapu, L.; Pastoriza-Santos, I.; Xu, Q.-H. Plasmon-Enhanced Light Harvesting: Applications in Enhanced Photocatalysis, Photodynamic Therapy and Photovoltaics. *RSC Adv.* **2015**, *5* (37), 29076–29097. https://doi.org/10.1039/C5RA01819F.

(17) Jia, C.; Li, X.; Xin, N.; Gong, Y.; Guan, J.; Meng, L.; Meng, S.; Guo, X. Interface-Engineered Plasmonics in Metal/Semiconductor Heterostructures. *Adv. Energy Mater.* **2016**, *6* (17), 1600431. https://doi.org/10.1002/aenm.201600431.

(18) Zhang, N.; Han, C.; Fu, X.; Xu, Y.-J. Function-Oriented Engineering of Metal-Based Nanohybrids for Photoredox Catalysis: Exerting Plasmonic Effect and Beyond. *Chem* **2018**, *4* (8), 1832–1861. https://doi.org/10.1016/j.chempr.2018.05.005.

(19) Li, J.; Cushing, S. K.; Zheng, P.; Meng, F.; Chu, D.; Wu, N. Plasmon-Induced Photonic and Energy-Transfer Enhancement of Solar Water Splitting by a Hematite Nanorod Array. *Nat. Commun.* **2013**, *4* (1), 2651. https://doi.org/10.1038/ncomms3651.

(20) Cushing, S. K.; Wu, N. Progress and Perspectives of Plasmon-Enhanced Solar Energy Conversion. *J. Phys. Chem. Lett.* **2016**, *7* (4), 666–675. https://doi.org/10.1021/acs.jpclett.5b02393.

(21) Xiao, F.-X.; Liu, B. Plasmon-Dictated Photo-Electrochemical Water Splitting for Solar-to-Chemical Energy Conversion: Current Status and Future Perspectives. *Adv. Mater. Interfaces* **2018**, *5* (6), 1701098. https://doi.org/10.1002/admi.201701098.

(22) Kholmicheva, N.; Royo Romero, L.; Cassidy, J.; Zamkov, M. Prospects and Applications of Plasmon-Exciton Interactions in the near-Field Regime. *Nanophotonics* **2019**, *8* (4), 613–628. https://doi.org/10.1515/nanoph-2018-0143.

(23) Ye, W.; Long, R.; Huang, H.; Xiong, Y. Plasmonic Nanostructures in Solar Energy Conversion. *J. Mater. Chem. C* **2017**, *5* (5), 1008–1021. https://doi.org/10.1039/C6TC04847A.

(24) Encina, E. R.; Coronado, E. A. Keys for Designing Hematite/Plasmonic Metal Hybrid Nanostructures with Enhanced Photoactive Properties. *J. Phys. Chem. C* **2018**, *122* (8), 4589–4599. https://doi.org/10.1021/acs.jpcc.7b12486.

(25) Cushing, S. K.; Chen, C.-J.; Dong, C. L.; Kong, X.-T.; Govorov, A. O.; Liu, R.-S.; Wu, N. Tunable Nonthermal Distribution of Hot Electrons in a Semiconductor Injected from a Plasmonic Gold Nanostructure. *ACS Nano* **2018**, *12* (7), 7117–7126. https://doi.org/10.1021/acsnano.8b02939.

(26) Cushing, S. K.; Li, J.; Bright, J.; Yost, B. T.; Zheng, P.; Bristow, A. D.; Wu, N. Controlling Plasmon-Induced Resonance Energy Transfer and Hot Electron Injection Processes in Metal@TiO 2 Core–Shell Nanoparticles. *J. Phys. Chem. C* **2015**, *119* (28), 16239–16244. https://doi.org/10.1021/acs.jpcc.5b03955.

(27) Khan, M. R.; Chuan, T. W.; Yousuf, A.; Chowdhury, M. N. K.; Cheng, C. K. Schottky Barrier and Surface Plasmonic Resonance Phenomena towards the Photocatalytic Reaction: Study of Their Mechanisms to Enhance Photocatalytic Activity. *Catal. Sci. Technol.* **2015**, *5* (5), 2522–2531. https://doi.org/10.1039/C4CY01545B.

(28) Pande, S.; Jana, S.; Sinha, A. K.; Sarkar, S.; Basu, M.; Pradhan, M.; Pal, A.; Chowdhury, J.; Pal, T. Dopamine Molecules on Aucore-Agshell Bimetallic Nanocolloids: Fourier Transform Infrared, Raman, and Surface-Enhanced Raman Spectroscopy Study Aided by Density Functional Theory. *J. Phys. Chem. C* **2009**, *113* (17), 6989–7002. https://doi.org/10.1021/jp810210a.

(29) Le Ru, E. C.; Blackie, E.; Meyer, M.; Etchegoint, P. G. Surface Enhanced Raman Scattering Enhancement Factors: A Comprehensive Study. *J. Phys. Chem. C* **2007**, *111* (37), 13794–13803. https://doi.org/10.1021/jp0687908.

(30) Le Ru, E. C.; Meyer, M.; Blackie, E.; Etchegoin, P. G. Advanced Aspects of Electromagnetic SERS Enhancement Factors at a Hot Spot. *J. Raman Spectrosc.* **2008**, *39* (9), 1127–1134. https://doi.org/10.1002/jrs.1945.

(31) Ahn, T.; Kim, J. H.; Yang, H.-M.; Lee, J. W.; Kim, J.-D. Formation Pathways of Magnetite Nanoparticles by Coprecipitation Method. *J. Phys. Chem. C* **2012**, *116* (10), 6069–6076. https://doi.org/10.1021/jp211843g.

(32) Baumgartner, J.; Dey, A.; Bomans, P. H. H.; Le Coadou, C.; Fratzl, P.; Sommerdijk, N. A. J. M.; Faivre, D. Nucleation and Growth of Magnetite from Solution. *Nat. Mater.* **2013**, *12* (4), 310–314. https://doi.org/10.1038/nmat3558.

(33) Thomas, G.; Demoisson, F.; Heintz, O.; Geoffroy, N.; Saviot, L.; Millot, N. Functionalized Fe 3 O 4 Nanoparticles: Influence of Ligand Addition Sequence and PH during Their Continuous Hydrothermal Synthesis. *RSC Adv.* **2015**, *5* (96), 78614–78624. https://doi.org/10.1039/C5RA17452J.

(34) Sugimoto, T.; Matijević, E. Formation of Uniform Spherical Magnetite Particles by Crystallization from Ferrous Hydroxide Gels. *J. Colloid Interface Sci.* **1980**, *74* (1), 227–243. https://doi.org/10.1016/0021-9797(80)90187-3.

(35) Vereda, F.; de Vicente, J.; Hidalgo-Alvarez, R. Oxidation of Ferrous Hydroxides with Nitrate: A Versatile Method for the Preparation of Magnetic Colloidal Particles. *J. Colloid Interface Sci.* **2013**, *392* (1), 50–56. https://doi.org/10.1016/j.jcis.2012.09.064.

(36) Lyon, J. L.; Fleming, D. A.; Stone, M. B.; Schiffer, P.; Williams, M. E. Synthesis of Fe Oxide Core/Au Shell Nanoparticles by Iterative Hydroxylamine Seeding. *Nano Lett.* **2004**, *4* (4), 719–723. https://doi.org/10.1021/nl035253f.

(37) Sun, H.; Jiao, X.; Han, Y.; Jiang, Z.; Chen, D. Magnetic Core / Shell Fe 3 O 4 / Au and Fe 3 O 4 / Au / Ag Nanoparticles with Tunable Plasmonic Properties. *J. Am. Chem. Soc.* **2007**, *129* (iii), 8698–8699.

(38) Salihov, S. V.; Ivanenkov, Y. A.; Krechetov, S. P.; Veselov, M. S.; Sviridenkova, N. V.; Savchenko, A. G.; Klyachko, N. L.; Golovin, Y. I.; Chufarova, N. V.; Beloglazkina, E. K.; et al. Recent Advances in the Synthesis of Fe 3 O 4 @AU Core/Shell Nanoparticles. *J. Magn. Magn. Mater.* **2015**, *394*, 173–178. https://doi.org/10.1016/j.jmmm.2015.06.012.

(39) Mishra, P.; Patnaik, S.; Parida, K. An Overview of Recent Progress on Noble Metal Modified Magnetic Fe 3 O 4 for Photocatalytic Pollutant Degradation and H 2 Evolution. *Catal. Sci. Technol.* **2019**, *9* (4), 916–941. https://doi.org/10.1039/C8CY02462F.

(40) Ingram, D. B.; Christopher, P.; Bauer, J. L.; Linic, S. Predictive Model for the Design of Plasmonic Metal/Semiconductor Composite Photocatalysts. *ACS Catal.* **2011**, *1* (10), 1441–1447. https://doi.org/10.1021/cs200320h.

(41) DDSCAT, http://ddscat.wikidot.com, (accessed September 2019).

(42) Draine, B. T.; Flatau, P. J. Discrete-Dipole Approximation For Scattering Calculations. *J. Opt. Soc. Am. A* **1994**, *11* (4), 1491. https://doi.org/10.1364/JOSAA.11.001491.

(43) Flatau, P. J.; Draine, B. T. Fast near Field Calculations in the Discrete Dipole Approximation for Regular Rectilinear Grids. *Opt. Express* **2012**, *20* (2), 1247. https://doi.org/10.1364/OE.20.001247.

(44) Palik, E. D. *Handbook of Optical Constant of Solids*, Academic P.; New york, 1895.

(45) Goossens, V.; Wielant, J.; Van Gils, S.; Finsy, R.; Terryn, H. Optical Properties of Thin Iron Oxide Films on Steel. *Surf. Interface Anal.* **2006**, *38* (4), 489–493. https://doi.org/10.1002/sia.2219.

(46) Vikesland, P. J.; Rebodos, R. L.; Bottero, J. Y.; Rose, J.; Mason, A. Aggregation and Sedimentation of Magnetite Nanoparticle Clusters. *Environ. Sci. Nano* **2016**, *3* (3), 567–577.

https://doi.org/10.1039/C5EN00155B.

(47) Brullot, W.; Valev, V. K.; Verbiest, T. Magnetic-Plasmonic Nanoparticles for the Life Sciences: Calculated Optical Properties of Hybrid Structures. *Nanomedicine Nanotechnology, Biol. Med.* **2012**, *8* (5), 559–568. https://doi.org/10.1016/j.nano.2011.09.004.

(48) Lim, J.; Eggeman, A.; Lanni, F.; Tilton, R. D.; Majetich, S. A. Synthesis and Single-Particle Optical Detection of Low-Polydispersity Plasmonic-Superparamagnetic Nanoparticles. *Adv. Mater.* **2008**, *20* (9), 1721–1726. https://doi.org/10.1002/adma.200702196.

(49) Li, J.; Cushing, S. K.; Bright, J.; Meng, F.; Senty, T. R.; Zheng, P.; Bristow, A. D.; Wu, N. Ag@Cu 2 O Core-Shell Nanoparticles as Visible-Light Plasmonic Photocatalysts. *ACS Catal.* **2013**, *3* (1), 47–51. https://doi.org/10.1021/cs300672f.

(50) Hashmi, A. S. K. Gold-Catalyzed Organic Reactions. *Chem. Rev.* **2007**, *107* (7), 3180–3211. https://doi.org/10.1021/cr000436x.

(51) Haruta, M. Size- and Support-Dependency in the Catalysis of Gold. *Catal. Today* **1997**, *36* (1), 153–166. https://doi.org/10.1016/S0920-5861(96)00208-8.

(52) Corma, A.; Garcia, H. Supported Gold Nanoparticles as Catalysts for Organic Reactions. *Chem. Soc. Rev.* **2008**, *37* (9), 2096. https://doi.org/10.1039/b707314n.

TOC Image

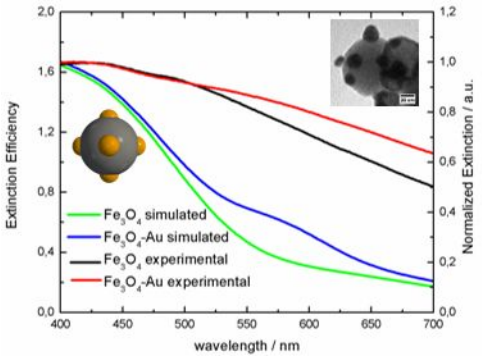
Extinction Efficiency
Normalized Extinction / a.u.
wavelength / nm
Fe3O4 simulated
Fe3O4-Au simulated
Fe3O4 experimental
Fe3O4-Au experimental